analytical chemistry

pubs.acs.org/ac Article

Profiling Cell−Matrix Adhesion Using Digitalized Acoustic Streaming

Hongwei Cai, Zheng Ao, Zhuhao Wu, Asael Nunez, Lei Jiang, Richard L. Carpenter, Kenneth P. Nephew, and Feng Guo*

Cite This: *Anal. Chem.* 2020, 92, 2283−2290 Read Online

ACCESS | Metrics & More | Article Recommendations | Supporting Information

ABSTRACT: Profiling the kinetics of cell−matrix adhesion is of great importance to understand many physiological and pathological processes such as morphogenesis, tissue homeostasis, wound healing, and tumorigenesis. Here, we developed a novel digital acoustofluidic device for parallel profiling cell−matrix adhesion at single-cell level. By introduction of localized and uniform acoustic streaming into an open chamber microfluidic device, the adherent cells within the open chamber can be detached by the streaming-induced Stokes drag force. By digital regulation of pulsed acoustic power from a low level to high levels, the hundreds of adherent cells can be ruptured from the fibronectin-coated substrate accordingly, and their adhesive forces (from several pN to several nN) and kinetics can be determined by the applied power and cell incubation time. As a proof-of-concept application for studying cancer metastasis, we applied this technique to measure the adhesion strength and kinetics of human breast cancer cells to extracellular matrix such as fibronectin and compared their metastatic potentials by measuring the rupture force of cancer cells representing malignant (MCF-7 cells and MDA-MB-231 cells) and nonmalignant (MCF-10A cells) states. Our acoustofluidic device is simple, easy to operate, and capable of measuring, in parallel, hundreds of individual cells' adhesion forces with a resolution at the pN level. Thus, we expect this device could be widely used for both fundamental cell biology research as well as development of cancer diagnostics and tissue engineering technologies.

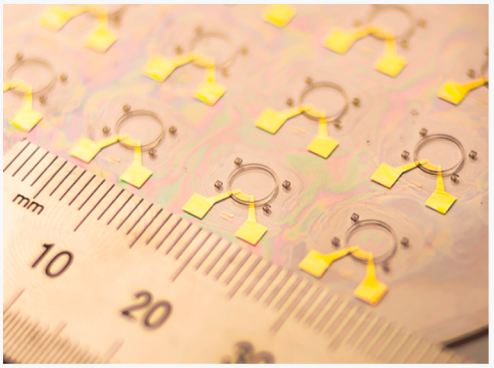

Investigation of cell−matrix adhesion is fundamentally important for basic biomedical research and translational medicine. Mammalian cells relay on their binding to tissue extracellular matrix (ECM) to obtain structural support.[1,2] Moreover, the cell−matrix interaction also plays a crucial role in regulating key cellular functions, including cell migration, differentiation, proliferation, and gene expression.[3−5] Thus, cell−matrix adhesion not only impacts tissue development and orogenesis but also pathological processes such as inflammation,[6] tumor growth,[7,8] and cancer metastasis.[9] Among these processes, cancer metastasis remains the greatest challenge in the clinical management of cancer, accounting for the majority of cancer-related mortality.[10] During cancer metastasis, circulating tumor cells (CTCs) released from primary tumors intravasate the vasculature of normal tissue, which allows CTCs to establish themselves at distant locations and form metastases.[11−13] Adhesion of CTCs to the endothelium ECM is a key step for tumor metastasis colonization. Moreover, it has been known for over a decade that the number of CTCs far exceeds the number of overt metastatic lesions that develop.[14−17] Adequate models and methods have impeded investigation of the molecular and cellular events during metastatic colonization. Therefore, exploring the adhesive interactions between CTCs and the ECM may potentially lead to the development of novel diagnostics as well as novel targets to treat or prevent metastasis.

To date, many efforts have been made to profile cell−matrix adhesion force by using conventional methods. One of the most commonly used techniques for the quantitative measurement of cell−matrix adhesion is atomic force microscopy (AFM).[18] Typically, one can immobilize a single living cell at the cantilever tip of AFM and use it as a measuring probe to measure the force and kinetics of cell detachment by setting this single cell in contact with the matrix surfaces for a defined time. Moreover, micropipette aspiration has been widely used to directly quantify cell−substrate adhesion force by applying a constant-rate aspiration pressure to rupture a single adhered cell from the matrix.[19] Surface plasmon resonance (SPR) technology is particularly suitable for real-time and label-free investigation of cell−substrate interactions by measuring the local refractive index distribution.[20,21] These methods are very sensitive and capable of providing real-time and high spatial

Received: November 6, 2019
Accepted: December 27, 2019
Published: December 27, 2019

https://dx.doi.org/10.1021/acs.analchem.9b05065
Anal. Chem. 2020, 92, 2283−2290

resolution information on cell−substrate interaction at the single-cell level, but are limited in parallel by measuring a large number of cells. The high-throughput methods including fluid-flow devices,[22] shear-spinning disks,[23] and centrifugation[24] use shear force induced by hydrodynamic flow or centrifugation to detach adherent cells from the substrate by adjusting the applied forces. Despite these methods that enable measurements of large cell populations, they may not access the accurate measurement of rupture forces because of the lack of real-time imaging and precise force control with bulk setups and normally require a relatively large number of cells (e.g., tens of thousands to several millions). Current conventional cell−matrix adhesion measurements are still not suitable for the measurement of CTCs because they cannot simultaneously provide a high-precision measurement for a relatively low number of CTCs (several tens to several hundreds) within a short time period (e.g., several tens of minutes to an hour).

Recent development of microfluidics seems to have a promising potential for parallel profiling cell−matrix adhesion force at the single-cell level.[25] By tuning hydrodynamic flows in a microchannel, the cultured cells within the closed chamber can be detached by the hydrodynamic shear force under different conditions, and the cell detachment process can be captured simultaneously using a time-lapse microscope.[26−31] A current hydrodynamic-flow-based microfluidic method offers multiple advantages over previous conventional approaches such as high-throughput performance, a wide range of detachment force, low sample consumption, and compatibility with a real-time imaging system and other modules.[27] However, this hydrodynamic-flow-based microfluidic method is not ready for wide applications in basic biomedical research such as CTC−matrix adhesion studies for a few reasons. First of all, this hydrodynamic-flow-based microfluidic method cannot provide an accurate measurement of cell detachment because it is hard to timely adjust the flow rate in the microfluidic channel, and it may need several tens of seconds to stably increase from a low flow rate to a high one.[32,33] A continuous varying flow can induce a varying shear force so that one cannot precisely access the force for the detachment of single cells from a substrate. Second, the continuous (or slowly varying) hydrodynamic flow in the microfluidic channel provides not only a shear force for adherent cells but also a continuous (or changing) compress stress force for these cells, which limits the maximal shear force produced by this technique for cell detachment measurement.[34] The maximal shear force produced by this method has been reported as high as 1 nN.[25] Thus, for exploration of the cell−matrix interaction, there are still unmet needs for improving hydrodynamic-flow-based microfluidics.

Acoustofluidics[35−38] may be an alternative solution for addressing the challenges in measuring CTC−matrix interaction. By introduction of bulk acoustic waves or surface acoustic waves into a microfluidic channel/chamber, the acoustofluidic technique normally uses acoustic radiation force and Stokes drag force induced by acoustic streaming to manipulate biological particles or fluids.[35−40] Because of the unique nature of acoustic waves, the acoustofluidic technique can achieve various biomanipulations in a label-free, contactless, and highly biocompatible manner. The acoustic radiation force has been used to pattern, transport, separate, and sort cells and particles[41−45] for broad application in tissue engineering, regenerative medicine, drug screening, and disease detection and treatment. Recently, acoustic radiation force has also been used to profile cell adhesion strength. By generation of a vertical standing acoustic wave within a resonate chamber made by solid materials, the bulk acoustofluidic device uses the acoustic radiation force to parallelly rupture and levitate hundreds of individual adherent T cells from a fibronectin-coated substrate with a maximal force up to 1 nN.[46] This technique provides a superior measurement of cell−matrix interaction to the above conventional and hydrodynamic-flow-based microfluidic methods. However, the resonate chamber made by solid materials such as glass limits the oxygen and nutrients perfusion and does not mimic well a physiologically relevant environment for cell culture. The acoustic-streaming-based cell detachment may be a good candidate for exploring CTC−matrix adhesion. In general, acoustic streaming induces viscous attenuation to liquids and is very useful for robust manipulation in a low Reynolds number microfluidic setting.[47,48] Acoustic streaming has been widely utilized for various applications including pumping of liquids, mixing of liquids and particles, enrichment of particles and cells, sorting particles and cells, rotating cells and worms, and moving cells and droplets.[49−57] A droplet-based surface acoustic wave system has been developed to detach biological cells from a surface and sort cell types on the basis of different adhesive forces to the substrate.[58] However, there are still unmet needs for developing a simple and versatile method that can parallelly measure the cell adhesive force with a wide spectrum.

Recently, we developed a series of digital acoustofluidic devices[59−61] that mainly use digitally regulated acoustic streaming for generation, transportation, and fusion of droplets as well as pumping and mixing of liquids. For example, our digital acoustofluidic pump can precisely tune flow rate from 0 to 41.5 nL/min within a response time of less than 1 s, showing a great potential for addressing the slowly varying flow rate issue in hydrodynamic-flow-based microfluidics.[59] Herein, we developed a novel digital acoustofluidic device for massively parallel profiling the strength and kinetics of cell−matrix adhesion at the single-cell level. Taking advantage of digitalized acoustic streaming generated with our digital acoustofluidic device, we can detach the hundreds of adherent cells cultured in an open chamber using precisely controlled forces with a force switching time of less than 100 ms and a force spectrum up to 10 nN. As a proof-of-concept application, we demonstrated how this digital acoustofluidic device can be used to profile the adherence strength and metastasis potential of different types of malignant and nonmalignant human breast cells.

EXPERIMENTAL SECTION

Cell Culture. Breast cancer cells (MCF-7, MDA-MB-231, and MCF-10A) were purchased from American Type Cell Culture (ATCC, Manassas, VA, USA) and cultured in Dulbecco's modified Eagle's medium (Corning, NY, USA) supplemented with 10% fetal bovine serum (Sigma-Aldrich, St. Louis, MO, USA), 100 U/mL penicillin, and 100 μg/mL streptomycin (Invitrogen, Millersburg, PA, USA) in a humidified incubator at 5% CO_2 and 37 °C.

Device Design and Fabrication. The device was designed and fabricated using the protocol that we developed previously.[62−66] The focused interdigital transducer (IDTs) was fabricated using a standard soft-lithography and lift-off technique. The focused IDTs were designed as 8 pairs of finger electrodes with the same finger width and gap ($\lambda/4$ = 25 μm) and a 57° focusing angle, and made by depositing two metal

https://dx.doi.org/10.1021/acs.analchem.9b05065
Anal. Chem. 2020, 92, 2283−2290

layers (Cr/Au with a thickness of 100 nm/500 nm) on a 128° YX-propagation lithium niobate substrate (with a thickness of 500 μm, double-side polished). Then the final device was made by fabricating a circular-shaped SU8 photoresist pattern (with a diameter of 4 mm, a wall thickness of 100 μm, and a thickness of 200 μm) on the same substrate using standard soft lithography.

Live/Dead Staining. Live/dead staining was conducted using the Live/Dead Kit (Invitrogen) following the manufacturer's instructions. The cells were stained in a medium supplemented with 2 μM carboxyfluorescein succinimidyl ester and 4 μM ethidium homodimer for 4 h. And the cells were cultured in the device for 30 min and the adhesion strength was measured (from 6 to 51 peak-to-peak voltage (Vpp), 3 Vpp interval). The staining results were visualized by an inverted fluorescence microscope (IX81, Olympus). Final cell viability was analyzed using ImageJ to account for area of live/dead cells.

RESULTS

Device Design and Working Principle. We developed a novel digital acoustofluidic device for massive parallel profiling cell−matrix adhesion at the single-cell level. The acoustofluidic device consists of a focused IDT and a circular-shaped open chamber fabricated atop a transparent lithium niobate (LiN_bO_3) substrate (Figure 1a,b). Once the focused IDT

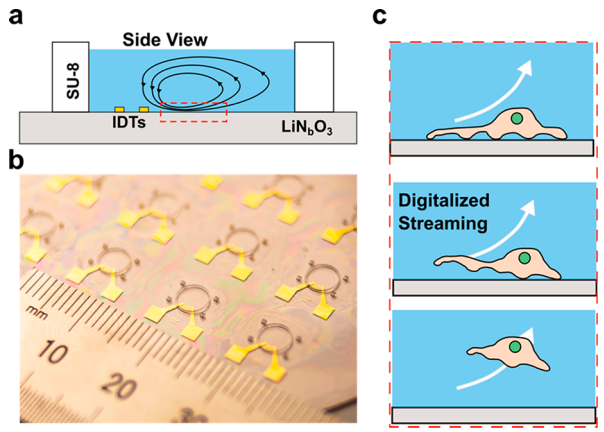

Figure 1. Digital acoustofluidic device for cell−matrix adhesion measurement. (a, b) Schematics (side view) and micrograph of our digital acoustofluidic device. The device consists of a focused IDT and an open microfluidic chamber fabricated on a transparent lithium niobate (LiN_bO_3) substrate. The pattern and direction of digitalized acoustic streaming are indicated by counterclockwise vortexes and arrows, respectively. (c) Illustration shows the detachment process of an adherent cell by digitalized acoustic streaming.

was activated at a resonance frequency of 37.4 MHz, a localized acoustic field was produced in the liquid domain above the IDT. Subsequently, highly localized acoustic streaming was also induced via the interface of the piezoelectric substrate and liquids. The Stokes drag force generated by the acoustic streaming ruptured the cell−matrix junction and detached cells from the fibronectin-functionalized substrate (Figure 1c). The localized streaming can offer uniform distributed streaming fields so that it can provide uniform shear force for all the cells within this area. By generation of digitalized streaming via a programmable radio frequency (RF) signal, Stokes drag force with precise control of the force level and duration can be produced and applied to the adherent cells within the area of interest to detach the cell from the substrate. Taking advantage of time-lapse imaging, the cell adhesive force to the substrate can be measured by recording and analyzing cell detachment and Stokes drag force induced by digitalized streaming. As a result, detailed force maps of cell−matrix interactions were measured during the process of acoustofluidic detachment. Because of the unique design of our digital acoustofluidic device, this technique can provide several advantages. Our device can generate uniform and localized acoustic streaming by introducing a focused IDT within an open microfluidic chamber. This design can reduce the acoustic energy loss and acoustic interference with the microfluidic channel well. By integration with a programmable RF signal, this device can generate a wide range of streaming speeds up to 10 mm/s and a short dynamic response time of less than 100 ms. Thus, our device can provide a measure of cell−matrix adhesion with a force range up to several nN and a force switching time less than 100 ms, which is better than previous acoustic radiation force-based or hydrodynamic-flow-based microfluidic methods. By use of an open microfluidic chamber, our device is compatible with conventional cell culture.

Acoustic Streaming. To profile the cell−matrix interaction, it is important to understand the mechanism by which focused IDTs detach cells from the substrate. In our experimental system, we used a simple device consisting of a focused IDT and a SU8 ring to investigate the mechanism of cell detachment. A set of traveling surface acoustic waves (SAWs) as a Rayleigh wave was produced after applying an RF signal to the focused IDT. The exponential decay of the amplitude with the depth of the substrate allowed the wave to confine most of its energy to the surface. Once the wave interfered with the liquid within the open chamber, localized streaming was created in the liquid. A numerical model was used to predict the three-dimensional pattern of acoustic streaming (Supporting Information). This model considered the effects of the transverse and longitudinal vibrations on the liquid and the interface between the substrate and the liquid layer in the chamber. Both the transverse and longitudinal vibrations attenuate in a thin boundary layer close to the substrate, resulting in a specific streaming pattern in the fluidic layer. Our numerical results described the streaming vortex and the distribution in three dimensions. The schematic and simulation of the acoustic streaming were described in Figure 2a,b. The arrows show the acoustic streaming direction, with streaming velocity indicated by background colors red (maximum) and blue (minimum). Along the vertical direction, the acoustic streaming flowed down the edge of the focused IDT, rotated counterclockwise, rose from the substrate, and then formed two streaming vortexes. Along the horizontal direction, two symmetric fluids jetted along the symmetric axis of the IDT from the edge of electrodes, interacted with the side boundary, recirculated back along the electrodes of the IDT, and then completed a second round of the streaming pattern.

With the guidance of our numerical prediction, we performed an experiment to investigate SAW-induced acoustic streaming within the fluidic chamber. We started the experiment by introducing 2 μm fluorescent polystyrene particles to the device. The particles were first uniformly located on the surface of the substrate. Once the SAW was applied, the particles were flowing to form two symmetric streaming vortexes along the symmetric axis of the IDT in the

https://dx.doi.org/10.1021/acs.analchem.9b05065
Anal. Chem. 2020, 92, 2283−2290

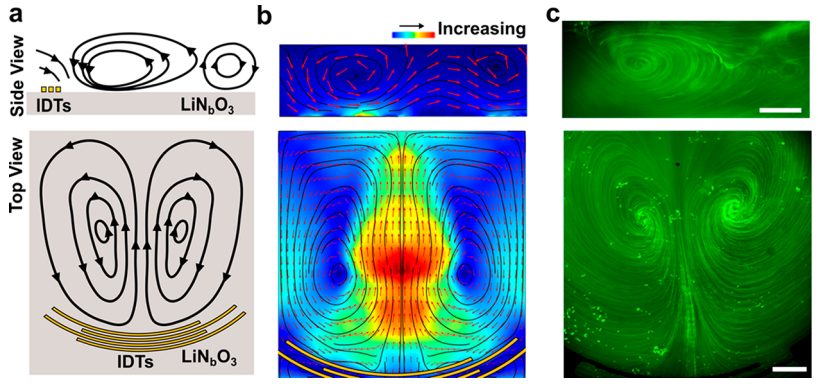

Figure 2. Acoustic streaming pattern. (a) Schematics show the top view and side view of the streaming pattern in an acoustofluidic device. The streaming flows down to the edge of the focused IDT along the $y-z$ plane, rotate counterclockwise back to the focused IDT, and form a streaming vortex. Two symmetric fluids jet along the symmetric axis of the IDT on the $x-y$ plane from the center of the electrode, interact with the side boundary, recirculate back to the sides of the IDT, and finally complete a two-vortex streaming pattern. (b) Simulation results show the side view and top view of the acoustic streaming pattern. The arrows indicate the streaming direction whereas the background colored with blue and red maps the streaming speed. (c) Experimental results show the acoustic streaming pattern by tracking the trajectories of 2 μm polystyrene particles (Movie S1-side view and Movie S2-top view). This region corresponds to the area of the simulation results. (Scale bar = 200 μm.)

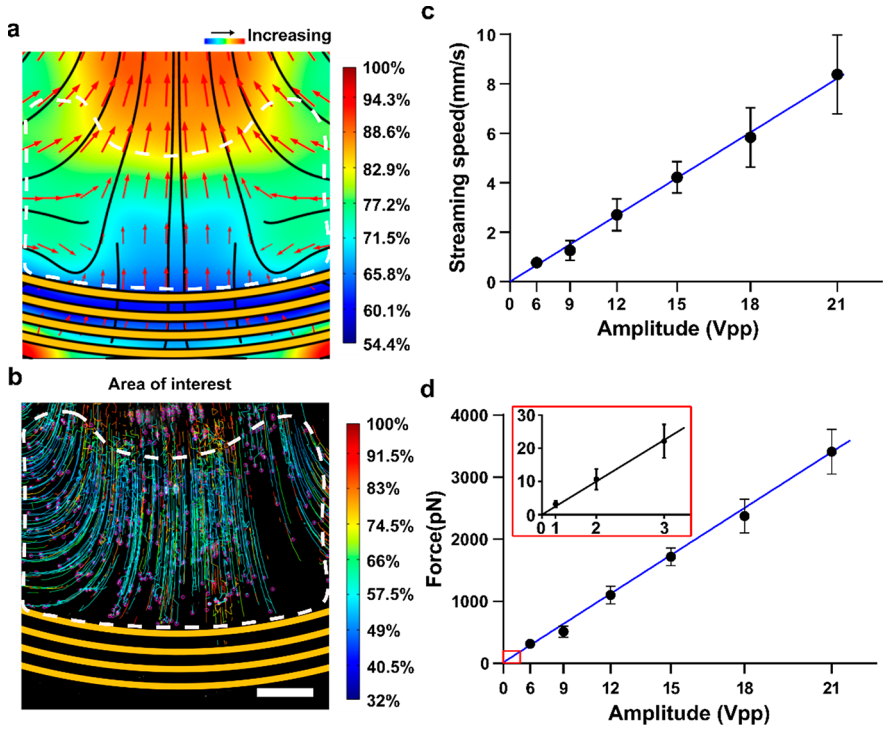

Figure 3. Streaming analysis. (a) Simulation of acoustic streaming field in the area of interest (AOI). The arrows indicate the streaming direction whereas the background colored with blue and red maps the streaming speed. The AOI is labeled with a white dashed line and uniform streaming speed (light green colored background) is located inside this area. (b) Experimental results of streaming in the AOI (labeled with a white dashed line). The colored lines map the trajectory of 2 μm polystyrene particles and the color indicates the streaming speed. Within the AOI, 2 μm polystyrene particles have similar speeds (light green). (c) Experimental results describe the dependence of the acoustic streaming speed on the input amplitude. The blue curve shows the quadratic fitted curve. (d) Dependence of Stokes drag force (calculated from the experimental acoustic streaming speed results) on acoustic power. The inset shows the Stokes drag force at a low amplitude level. (Scale bar = 50 μm.)

$x-y$ plane (Movie S1). A time series of frames captured from the movie were superimposed to show the streaming pattern (Figure 2c, side view). Along the vertical axis, a triprism was used to help visualize the movement of particles. The microscope was focused on the symmetric axis of the focused IDT. Once the SAW was applied, the particles rose up from the substrate, rotated counterclockwise, flowed down to the focused IDT, and formed a vortex (Movie S2). A time series of frames captured from the movie were superimposed to show the streaming pattern (Figure 2c, top view).

Force Analysis. To calculate the rupture force of the cell–matrix junction by acoustic streaming, we must quantify the streaming speeds of different RF signal voltage inputs. First, an area with uniformly distributed streaming must be determined. Numerical results showed a scalloped area close to the focused IDT, with an almost identically colored streaming pattern (Figure 3a, light green). We validated our numerical prediction

https://dx.doi.org/10.1021/acs.analchem.9b05065
Anal. Chem. 2020, 92, 2283−2290

with the experiment using the aforementioned device. Fluorescent polystyrene particles were used as markers to trace streaming patterns. A sequence of images was captured using a CMOS camera at time intervals of 10 ms (100 fps). The streaming speed was then analyzed and calculated by the Trackmate plugin of ImageJ software. Trajectories of particles with the color of trajectories showing the streaming speed distribution (red, maximum; blue, minimum) can be seen in Figure 3b. In the experimental results, evenly distributed streaming (light green in color) appeared in the same area as the numerical results predicted. As a result, an area of interest (AOI; dashed white line, Figure 3a,b) was employed to profile the cell−matrix interaction.

To further quantify the acoustic streaming, we investigated the dependence of the streaming speed in AOI on the input Vpp. We tracked particles in AOI under different signal amplitude inputs for five repetitions and calculated the average streaming speed and standard deviation (trajectories last for at least 5 frames). The final streaming speed versus input amplitude was plotted (Figure 3c), which showed that trapping velocities increased gradually in a squared trend as the input peak-to-peak voltage increased. Because the maximum frame rate of the camera was 100 fps, when the streaming speed was too high, beads could not be tracked. The streaming speed has a squared relationship with amplitude input, and our experimental results showed the squared trend. The curve was fitted quadratically to account for streaming speed when the amplitude was larger than 21 Vpp. Monitoring of the streaming speed can be achieved by tuning the amplitude of the input signal. To determine the adherence strength of cells using our acoustofluidic detachment method, we calculated the Stokes drag force on cells under different amplitude inputs (for details, see Supporting Information, force calculation). The calculated Stokes drag force on adherent cells versus amplitude input is shown in Figure 3d.

Measurement of Cell−Matrix Adhesion. On the basis of our numerical and experimental results of an acoustic streaming field, we further detached the adherent MDA-MB-231 cells from a fibronectin-functionalized substrate. The chambers were coated with fibronectin to mimic the ECM lining the endothelium of blood vessels.[67] MDA-MB-231 cells were loaded into the chamber and allowed to settle down on the fibronectin-coated bottom surface. After a 1-h incubation, a pulse surface acoustic wave (frequency = 37.4 MHz, power = 57 Vpp, duration = 1.5 s, about 16 nN) was applied to detach adherent cells. After a 1-h culture, MDA-MB-231 cells first adhered and then spread out on the fibronectin-coated surface (Figure 4). When the SAW was applied to the device, a strong localized streaming was generated in the fluid domain. Stokes drag force induced by the flow gradually detached the cells in the streaming field, and all adherent cells were detached within 1 s. The viability of MCF-7 cells was tested as (82.3 ± 5.4%) before the acoustic detachment and as (79.8 ± 7.5%) after the acoustic detachment (Figure S2).

We conclude that localized streaming is capable of detaching fully adherent cells on the fibronectin-coated surface and has good biocompatibility.

Kinetics of Cell−Matrix Adhesion. After successfully measuring the cell adhesive force, we explored the kinetics of cell−matrix adhesion of MCF-7 breast cancer cells using our method. To quantify the kinetics of tumor cell adhesion to fibronectin, we applied a 1.5-s acoustic pulse every 3 s and gradually increased the amplitude of each pulse at the interval

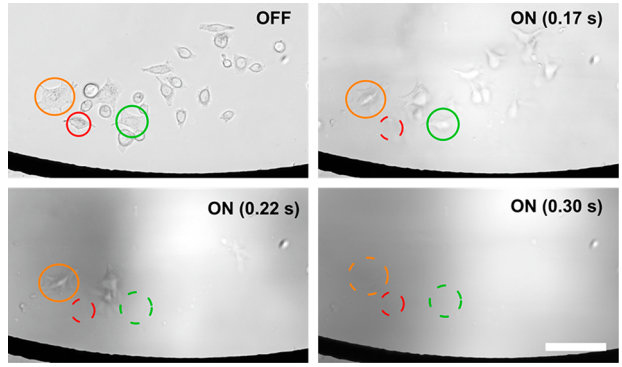

Figure 4. Cell detachment. Acoustofluidic detachment process of adherent (MDA-MB-231) breast cancer cells (Movie S3). When the digitalized streaming was applied, all the adherent cells detached from the substrate with one pulse (frequency = 37.4 MHz; duration = 1.5 s; amplitude = 57 Vpp). When the solid circle became dashed, the labeled cells were detached at the corresponding time point. (Scale bar = 200 μm.)

of 3 Vpp starting from 6 Vpp to track the force map of all tumor cells (Figure 5a). During the detachment process, we continuously imaged the cells and quantified the number of detached cells after each pulse. Using this approach, we typically measured the detailed rupture force of several hundreds of cells for one measurement. We cultured MCF-7 cells for 10, 20, and 30 min and then measured rupture forces of these cells (Movie S4). The detachment process of MCF-7 cells (after a 30-min incubation) was shown in Figure 5a. The cells were attached to the substrate at the beginning, and as we gradually increased the pulse signal amplitude input, cells gradually detached. After the amplitude reached 51 Vpp (about 12 nN), all cells were detached. The experiment was repeated five times at each time point, and the resulting rupture force distribution of MCF-7 cells under different culture times were plotted (Figure 5b), showing a clear correlation of time in culture with increased rupture force.

Characterization of Metastatic Potential. Although adhesion of CTCs to endothelial ECM is a critical step in the tumor metastasis process,[8] it is hard to know the dynamic adhesion force of CTCs during the metastatic process. We measured the dynamic adhesion force of MCF-10A (Movie S5), MCF-7 (Movie S6), and MDA-MB-231 (Movie S7) cells to fibronectin using our acoustic streaming detachment device. Using the aforementioned device and procedure, we cultured the three breast cancer lines for 15 min, measured rupture forces, and created rupture force maps. As shown in Figure 6, MDA-MB-231 cells (highly aggressive breast cancer cell line) adhered most strongly to the fibronectin-coated substrate, demonstrating that this cell line has the greatest metastatic potential. In comparison, the MCF-10A cell line (non-tumorigenic breast epithelial cell line) has the least metastatic potential, as these cells can be detached with the lowest acoustic amplitude input on our system. Adhesion analysis showed that MCF-7 cells, a poorly aggressive and noninvasive cell line, normally considered to have low metastatic potential, was between the MCF-10A and MDA-MB-231 cells (Figure 6).

CONCLUSIONS

In summary, we developed a novel digital acoustofluidic device to determine the interaction between cells and ECM using

https://dx.doi.org/10.1021/acs.analchem.9b05065
Anal. Chem. 2020, 92, 2283−2290

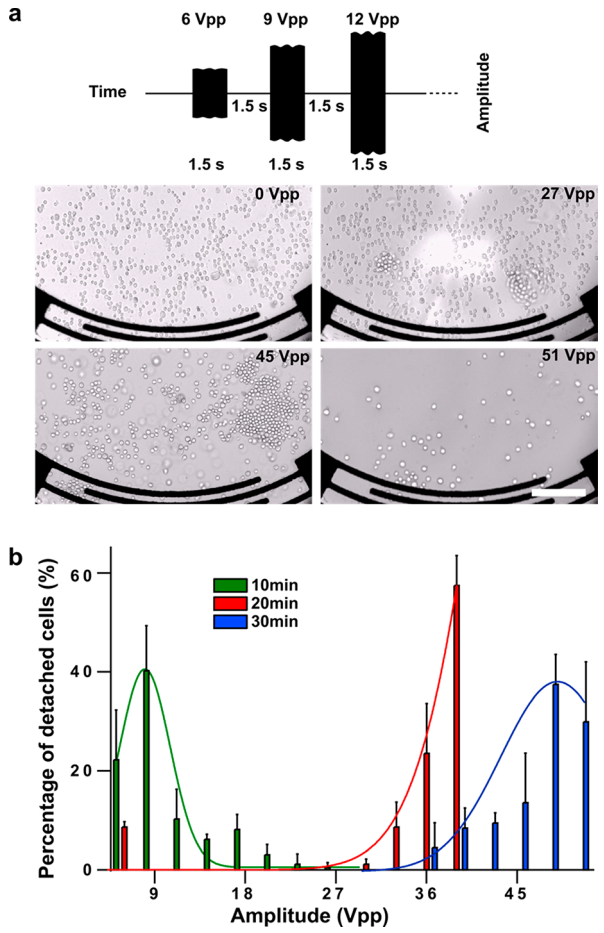

Figure 5. Kinetics of cell–matrix adhesion. (a) RF signal (frequency = 37.4 MHz; duration = 1.5 s; period = 3 s) was programmed to have an amplitude increase of 3 Vpp for each period (amplitude = 6, 9, 12, 15, ..., 51 Vpp), respectively (Movie S4). Time-elapsed images of the cell detachment process under different rupturing forces after MCF-7 cells adhered to fibronectin-coated substrate for 30 min. When the amplitude was up to 51 Vpp, all the adherent MCF-7 cells were detached. (b) Detached cells distribution of the acoustic amplitude (10-, 20-, and 30-min culture time). (Scale bar = 200 μm.)

localized acoustic streaming. The adherent cells were detached from the coated substrate by Stokes drag force induced by the strong uniform streaming. We believe that the novel acoustofluidic design used to profile the cell–matrix adhesion has great potential in a wide spectrum of biomedical applications. By tuning of the input amplitude, the acoustic streaming force can be tuned from hundreds of pN to tens of nN. Moreover, we showed that our acoustofluidic detachment technique can characterize the adhesion dynamics and kinetics of cancer cells to fibronectin. The observed differences in adhesion strength across different types of breast cancer cells demonstrate the broad application potential of our method. In conclusion, our acoustofluidic device is low-cost and able to analyze hundreds of cells in parallel, while maintaining high precision. Moreover, the user-friendly feature of our digitally controlled device could be used to develop cancer diagnostic tools and implantable devices as well as to study fundamental biology.

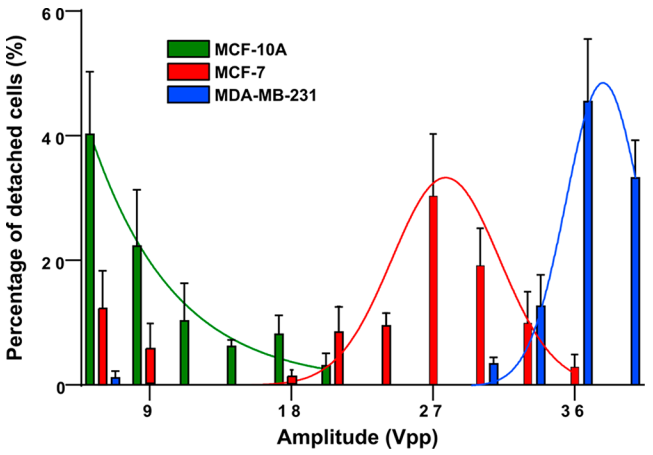

Figure 6. Metastasis measurement. Distribution of the detachment of different breast cancer cells (MCF-10A, Movie S5; MCF-7, Movie S6; and MDA-MB-231, Movie S7) to acoustic input amplitude was plotted. After a 15-min on-chip incubation, human breast cancer cells showed distant distribution patterns. The most malignant MDA-MB-231 cells distributed in a high amplitude range, whereas the most nonmalignant MCF-10A cells are in a low amplitude range.

■ ASSOCIATED CONTENT

Supporting Information

The Supporting Information is available free of charge at https://pubs.acs.org/doi/10.1021/acs.analchem.9b05065.

Acoustic streaming simulation, force calculation, sketch of the computational domain of the acoustofluidic device, and viability of cells after the acoustic detachment (PDF)

Movie S1: Tracking of streaming pattern (side view) using time-lapse imaging (MP4)

Movie S2: Tracking of streaming pattern (top view) using time-lapse imaging (MP4)

Movie S3: Experimental observation of adherent MCF-7 cells detaching from the substrate by acoustic streaming (MP4)

Movie S4: Detachment process of MCF-7 cells after a 30-min incubation (MP4)

Movie S5: Detachment process of MCF-7 cells after a 15-min incubation (MP4)

Movie S6: Detachment process of MDA-MB-231 cells after a 15-min incubation (MP4)

Movie S7: Detachment process of MCF-10A cells after a 15-min incubation (MP4)

■ AUTHOR INFORMATION

Corresponding Author

Feng Guo – *Indiana University, Bloomington, Indiana, and Melvin and Bren Simon Cancer Center, Indianapolis, Indiana;* orcid.org/0000-0001-9103-3235; Email: fengguo@iu.edu

Other Authors

Hongwei Cai – *Indiana University, Bloomington, Indiana*

Zheng Ao – *Indiana University, Bloomington, Indiana;* orcid.org/0000-0003-2569-0346

Zhuhao Wu – *Indiana University, Bloomington, Indiana*

Asael Nunez – *Indiana University, Bloomington, Indiana*

Lei Jiang – *Indiana University, Bloomington, Indiana*

https://dx.doi.org/10.1021/acs.analchem.9b05065
Anal. Chem. 2020, 92, 2283–2290

Richard L. Carpenter − *Indiana University School of Medicine, Bloomington, Indiana, and Melvin and Bren Simon Cancer Center, Indianapolis, Indiana*
Kenneth P. Nephew − *Indiana University School of Medicine, Bloomington, Indiana, and Melvin and Bren Simon Cancer Center, Indianapolis, Indiana*

Complete contact information is available at: https://pubs.acs.org/10.1021/acs.analchem.9b05065

Notes

The authors declare no competing financial interest.

■ ACKNOWLEDGMENTS

This project was funded the departmental start-up funds of Indiana University Bloomington, and partially supported by the National Science Foundation (CCF-1909509).

■ REFERENCES

(1) Huang, S.; Ingber, D. E. *Nat. Cell Biol.* **1999**, *1*, E131−E138.
(2) Bokel, C.; Brown, N. H. *Dev. Cell* **2002**, *3*, 311−321.
(3) Sun, J.; Zhang, L.; Wang, J.; Feng, Q.; Liu, D.; Yin, Q.; Xu, D.; Wei, Y.; Ding, B.; Shi, X.; Jiang, X. *Adv. Mater.* **2015**, *27*, 1402−1407.
(4) Streuli, C. *Curr. Opin. Cell Biol.* **1999**, *11*, 634−640.
(5) Danen, E. H.; Sonnenberg, A. *J. Pathol.* **2003**, *201*, 632−641.
(6) Livant, D. L.; Brabec, R. K.; Kurachi, K.; Allen, D. L.; Wu, Y.; Haaseth, R.; Andrews, P.; Ethier, S. P.; Markwart, S. *J. Clin. Invest.* **2000**, *105*, 1537−1545.
(7) Avraamides, C. J.; Garmy-Susini, B.; Varner, J. A. *Nat. Rev. Cancer* **2008**, *8*, 604−617.
(8) Weis, S. M.; Cheresh, D. A. *Nat. Med.* **2011**, *17*, 1359.
(9) Craig, S. E.; Brady-Kalnay, S. M. *Cancer Res.* **2011**, *71*, 303−309.
(10) Poudineh, M.; Labib, M.; Ahmed, S.; Nguyen, L. N.; Kermanshah, L.; Mohamadi, R. M.; Sargent, E. H.; Kelley, S. O. *Angew. Chem., Int. Ed.* **2017**, *56*, 163−168.
(11) Song, Y.; Tian, T.; Shi, Y.; Liu, W.; Zou, Y.; Khajvand, T.; Wang, S.; Zhu, Z.; Yang, C. *Chem. Sci.* **2017**, *8*, 1736−1751.
(12) Harouaka, R.; Kang, Z.; Zheng, S.-Y.; Cao, L. *Pharmacol. Ther.* **2014**, *141*, 209−221.
(13) Hao, S.; Ha, L.; Cheng, G.; Wan, Y.; Xia, Y.; Sosnoski, D. M.; Mastro, A. M.; Zheng, S.-Y. *Small* **2018**, *14*, 1702787.
(14) Lin, H. K.; Zheng, S.; Williams, A. J.; Balic, M.; Groshen, S.; Scher, H. I.; Fleisher, M.; Stadler, W.; Datar, R. H.; Tai, Y.-C.; Cote, R. J. *Clin. Cancer Res.* **2010**, *16*, 5011.
(15) Zheng, S.; Lin, H.; Liu, J.-Q.; Balic, M.; Datar, R.; Cote, R. J.; Tai, Y.-C. *J. of Chromatography A* **2007**, *1162*, 154−161.
(16) Xia, Y.; Wan, Y.; Hao, S.; Nisic, M.; Harouaka, R. A.; Chen, Y.; Zou, X.; Zheng, S.-Y. *Small* **2018**, *14*, 1802899.
(17) Massagué, J.; Obenauf, A. C. *Nature* **2016**, *529*, 298.
(18) Benoit, M.; Gabriel, D.; Gerisch, G.; Gaub, H. E. *Nat. Cell Biol.* **2000**, *2*, 313−317.
(19) Hogan, B.; Babataheri, A.; Hwang, Y.; Barakat, A. I.; Husson, J. *Biophys. J.* **2015**, *109*, 209−219.
(20) Yanase, Y.; Suzuki, H.; Tsutsui, T.; Hiragun, T.; Kameyoshi, Y.; Hide, M. *Biosens. Bioelectron.* **2007**, *22*, 1081−1086.
(21) Mrksich, M. *Chem. Soc. Rev.* **2000**, *29*, 267−273.
(22) Palange, A. L.; Di Mascolo, D.; Singh, J.; De Franceschi, M. S.; Carallo, C.; Gnasso, A.; Decuzzi, P. *Front. Oncol.* **2012**, *2*, 161.
(23) Friedland, J. C.; Lee, M. H.; Boettiger, D. *Science* **2009**, *323*, 642−644.
(24) Reyes, C. D.; García, A. J. *J. Biomed. Mater. Res., Part A* **2003**, *67A*, 328−333.
(25) Khalili, A. A.; Ahmad, R. M. *Int. J. Mol. Sci.* **2015**, *16*, 18149−18184.
(26) Young, E. W. K.; Wheeler, A. R.; Simmons, C. A. *Lab Chip* **2007**, *7*, 1759−1766.
(27) Lu, H.; Koo, L. Y.; Wang, W. M.; Lauffenburger, D. A.; Griffith, L. G.; Jensen, K. F. *Anal. Chem.* **2004**, *76*, 5257−5264.
(28) Zhang, X.; Jones, P.; Haswell, S. J. *Chem. Eng. J.* **2008**, *135*, S82−S88.
(29) Tang, Z.; Akiyama, Y.; Itoga, K.; Kobayashi, J.; Yamato, M.; Okano, T. *Biomaterials* **2012**, *33*, 7405−7411.
(30) Christ, K. V.; Williamson, K. B.; Masters, K. S.; Turner, K. T. *Biomed. Microdevices* **2010**, *12*, 443−455.
(31) Chen, Y.-C.; Baac, H. W.; Lee, K.-T.; Fouladdel, S.; Teichert, K.; Ok, J. G.; Cheng, Y.-H.; Ingram, P. N.; Hart, A. J.; Azizi, E.; Guo, L. J.; Wicha, M. S.; Yoon, E. *ACS Nano* **2017**, *11*, 4660−4668.
(32) Mavrogiannis, N.; Ibo, M.; Fu, X.; Crivellari, F.; Gagnon, Z. *Biomicrofluidics* **2016**, *10*, 034107−034107.
(33) Li, Z.; Mak, S. Y.; Sauret, A.; Shum, H. C. *Lab Chip* **2014**, *14*, 744−749.
(34) Mao, S.; Zhang, Q.; Li, H.; Zhang, W.; Huang, Q.; Khan, M.; Lin, J.-M. *Chem. Sci.* **2018**, *9*, 7694−7699.
(35) Friend, J.; Yeo, L. Y. *Rev. Mod. Phys.* **2011**, *83*, 647−704.
(36) Ozcelik, A.; Rufo, J.; Guo, F.; Gu, Y.; Li, P.; Lata, J.; Huang, T. J. *Nat. Methods* **2018**, *15*, 1021−1028.
(37) Ding, X.; Li, P.; Lin, S.-C. S.; Stratton, Z. S.; Nama, N.; Guo, F.; Slotcavage, D.; Mao, X.; Shi, J.; Costanzo, F.; Huang, T. J. *Lab Chip* **2013**, *13*, 3626−3649.
(38) Liu, S.; Ni, Z.; Xu, G.; Guo, X.; Tu, J.; Bruus, H.; Zhang, D. *Phys. Rev. Appl.* **2019**, *11*, 044031.
(39) He, M. H.; Zhou, Y. C.; Cui, W. W.; Yang, Y.; Zhang, H. X.; Chen, X. J.; Pang, W.; Duan, X. X. *Lab Chip* **2018**, *18*, 2540.
(40) Bruus, H.; Dual, J.; Hawkes, J.; Hill, M.; Laurell, T.; Nilsson, J.; Radel, S.; Sadhal, S.; Wiklund, M. *Lab Chip* **2011**, *11*, 3579−3580.
(41) Guo, F.; Li, P.; French, J. B.; Mao, Z.; Zhao, H.; Li, S.; Nama, N.; Fick, J. R.; Benkovic, S. J.; Huang, T. J. *Proc. Natl. Acad. Sci. U. S. A.* **2015**, *112*, 43.
(42) Ahmed, H.; Destgeer, G.; Park, J.; Jung, J. H.; Ahmad, R.; Park, K.; Sung, H. J. *Anal. Chem.* **2017**, *89*, 13575−13581.
(43) Magnusson, C.; Undvall, E.; Laurell, T.; Lilja, H. *Cancer Res.* **2018**, *78*, A027.
(44) Ai, Y.; Sanders, C. K.; Marrone, B. L. *Anal. Chem.* **2013**, *85*, 9126−9134.
(45) Cushing, K. W.; Garofalo, F.; Magnusson, C.; Ekblad, L.; Bruus, H.; Laurell, T. *Anal. Chem.* **2017**, *89*, 8917−8923.
(46) Kamsma, D.; Bochet, P.; Oswald, F.; Alblas, N.; Goyard, S.; Wuite, G. J. L.; Peterman, E. J. G.; Rose, T. *Cell Rep.* **2018**, *24*, 3008−3016.
(47) Destgeer, G.; Sung, H. J. *Lab Chip* **2015**, *15*, 2722−2738.
(48) Jung, J. H.; Destgeer, G.; Park, J.; Ahmed, H.; Park, K.; Sung, H. J. *RSC Adv.* **2018**, *8*, 3206−3212.
(49) Dentry, M. B.; Friend, J. R.; Yeo, L. Y. *Lab Chip* **2014**, *14*, 750−758.
(50) Patel, M. V.; Nanayakkara, I. A.; Simon, M. G.; Lee, A. P. *Lab Chip* **2014**, *14*, 3860−3872.
(51) Phan, H. V.; Coşkun, M. B.; Şeşen, M.; Pandraud, G.; Neild, A.; Alan, T. *Lab Chip* **2015**, *15*, 4206−4216.
(52) Luong, T.-D.; Phan, V.-N.; Nguyen, N.-T. *Microfluid. Nanofluid.* **2011**, *10*, 619−625.
(53) Collins, D. J.; Khoo, B. L.; Ma, Z.; Winkler, A.; Weser, R.; Schmidt, H.; Han, J.; Ai, Y. *Lab Chip* **2017**, *17*, 1769−1777.
(54) Garg, N.; Westerhof, T. M.; Liu, V.; Liu, R.; Nelson, E. L.; Lee, A. P. *Microsys Nanoengineer* **2018**, *4*, 17085.
(55) Franke, T.; Braunmüller, S.; Schmid, L.; Wixforth, A.; Weitz, D. A. *Lab Chip* **2010**, *10*, 789−794.
(56) Collins, D. J.; Ma, Z. C.; Ai, Y. *Anal. Chem.* **2016**, *88*, 5513−5522.
(57) Zhang, H.; Tang, Z. X.; Wang, Z.; Pan, S. T.; Han, Z. Y.; Sun, C. L.; Zhang, M. L.; Duan, X. X.; Pang, W. *Phys. Rev. Appl.* **2018**, *9*, 064011.
(58) Bussonnière, A.; Miron, Y.; Baudoin, M.; Bou Matar, O.; Grandbois, M.; Charette, P.; Renaudin, A. *Lab Chip* **2014**, *14*, 3556.
(59) Wu, Z.; Cai, H.; Ao, Z.; Nunez, A.; Liu, H.; Bondesson, M.; Guo, S.; Guo, F. *Anal. Chem.* **2019**, *91*, 7097−7103.

(60) Chen, K.; Sui, C.; Wu, Y.; Ao, Z.; Guo, S.-s.; Guo, F. *Nanotechnology* **2019**, *30*, 084001.
(61) Zhang, S. P.; Lata, J.; Chen, C.; Mai, J.; Guo, F.; Tian, Z.; Ren, L.; Mao, Z.; Huang, P.-H.; Li, P.; Yang, S.; Huang, T. J. *Nat. Commun.* **2018**, *9*, 2928.
(62) Guo, F.; Mao, Z.; Chen, Y.; Xie, Z.; Lata, J. P.; Li, P.; Ren, L.; Liu, J.; Yang, J.; Dao, M.; Suresh, S.; Huang, T. J. *Proc. Natl. Acad. Sci. U. S. A.* **2016**, *113*, 1522.
(63) Guo, F.; Xie, Y.; Li, S.; Lata, J.; Ren, L.; Mao, Z.; Ren, B.; Wu, M.; Ozcelik, A.; Huang, T. J. *Lab Chip* **2015**, *15*, 4517−4523.
(64) Lata, J. P.; Guo, F.; Guo, J.; Huang, P. H.; Yang, J.; Huang, T. J. *Adv. Mater.* **2016**, *28*, 8632−8638.
(65) Chen, B.; Wu, Y.; Ao, Z.; Cai, H.; Nunez, A.; Liu, Y.; Foley, J.; Nephew, K.; Lu, X.; Guo, F. *Lab Chip* **2019**, *19*, 1755−1763.
(66) Wu, Y.; Ao, Z.; Bin Chen; Muhsen, M.; Bondesson, M.; Lu, X.; Guo, F. *Nanotechnology* **2018**, *29*, 504006.
(67) Li, F.; Redick, S. D.; Erickson, H. P.; Moy, V. T. *Biophys. J.* **2003**, *84*, 1252−1262.

https://dx.doi.org/10.1021/acs.analchem.9b05065
Anal. Chem. 2020, 92, 2283−2290